

# Interface-engineered ferroelectricity of epitaxial $\text{Hf}_{0.5}\text{Zr}_{0.5}\text{O}_2$ thin films

Received: 27 October 2022

Accepted: 22 March 2023

Published online: 30 March 2023

Check for updates

Shu Shi<sup>1,11</sup>, Haolong Xi<sup>2,3,11</sup>, Tengfei Cao<sup>4,11</sup>, Weinan Lin<sup>5,11</sup>, Zhongran Liu<sup>3</sup>, Jiangzhen Niu<sup>6</sup>, Da Lan<sup>1</sup>, Chenghang Zhou<sup>1</sup>, Jing Cao<sup>7</sup>, Hanxin Su<sup>1</sup>, Tiegang Zhao<sup>1</sup>, Ping Yang<sup>8</sup>, Yao Zhu<sup>9</sup>, Xiaobing Yan<sup>6</sup>✉, Evgeny Y. Tsybal<sup>4</sup>✉, He Tian<sup>3,10</sup>✉ & Jingsheng Chen<sup>1</sup>✉

Ferroelectric hafnia-based thin films have attracted intense attention due to their compatibility with complementary metal-oxide-semiconductor technology. However, the ferroelectric orthorhombic phase is thermodynamically metastable. Various efforts have been made to stabilize the ferroelectric orthorhombic phase of hafnia-based films such as controlling the growth kinetics and mechanical confinement. Here, we demonstrate a key interface engineering strategy to stabilize and enhance the ferroelectric orthorhombic phase of the  $\text{Hf}_{0.5}\text{Zr}_{0.5}\text{O}_2$  thin film by deliberately controlling the termination of the bottom  $\text{La}_{0.67}\text{Sr}_{0.33}\text{MnO}_3$  layer. We find that the  $\text{Hf}_{0.5}\text{Zr}_{0.5}\text{O}_2$  films on the  $\text{MnO}_2$ -terminated  $\text{La}_{0.67}\text{Sr}_{0.33}\text{MnO}_3$  have more ferroelectric orthorhombic phase than those on the  $\text{LaSrO}$ -terminated  $\text{La}_{0.67}\text{Sr}_{0.33}\text{MnO}_3$ , while with no wake-up effect. Even though the  $\text{Hf}_{0.5}\text{Zr}_{0.5}\text{O}_2$  thickness is as thin as 1.5 nm, the clear ferroelectric orthorhombic (111) orientation is observed on the  $\text{MnO}_2$  termination. Our transmission electron microscopy characterization and theoretical modelling reveal that reconstruction at the  $\text{Hf}_{0.5}\text{Zr}_{0.5}\text{O}_2/\text{La}_{0.67}\text{Sr}_{0.33}\text{MnO}_3$  interface and hole doping of the  $\text{Hf}_{0.5}\text{Zr}_{0.5}\text{O}_2$  layer resulting from the  $\text{MnO}_2$  interface termination are responsible for the stabilization of the metastable ferroelectric phase of  $\text{Hf}_{0.5}\text{Zr}_{0.5}\text{O}_2$ . We anticipate that these results will inspire further studies of interface-engineered hafnia-based systems.

The discovery of ferroelectricity in Si-doped  $\text{HfO}_2$  thin films in 2011<sup>1</sup> has triggered extensive research and technological interest in this material. Due to robust ferroelectricity at reduced dimensions<sup>2–4</sup> and compatibility with complementary metal-oxide-semiconductor

(CMOS) technology, these films are promising for applications in ferroelectric-random access memories (FeRAMs), ferroelectric-field effect transistors (FeFET), and neuromorphic devices<sup>5–14</sup>. At high temperatures,  $\text{HfO}_2$  possesses a high-symmetry cubic phase ( $Fm\bar{3}m$ ),

<sup>1</sup>Department of Materials Science and Engineering, National University of Singapore, 117575 Singapore, Singapore. <sup>2</sup>School of Materials and Energy, Electron Microscopy Centre of Lanzhou University and Key Laboratory of Magnetism and Magnetic Materials of the Ministry of Education, Lanzhou University, Lanzhou 730000, PR China. <sup>3</sup>Center of Electron Microscope, State Key Laboratory of Silicon Materials, School of Materials Science and Engineering, Zhejiang University, Hangzhou 310027, China. <sup>4</sup>Department of Physics and Astronomy and Nebraska Center for Materials and Nanoscience, University of Nebraska, Lincoln, NE 68588-0299, USA. <sup>5</sup>Department of physics, Xiamen University, Xiamen 361005, China. <sup>6</sup>Key Laboratory of Brain-Like Neuromorphic Devices and Systems of Hebei Province, Hebei University, Baoding 071002, PR China. <sup>7</sup>Institute of Materials Research and Engineering, Agency for Science, Technology and Research (A\*STAR), 138634 Singapore, Singapore. <sup>8</sup>Singapore Synchrotron Light Source (SSLS), National University of Singapore, 5 Research Link, 117603 Singapore, Singapore. <sup>9</sup>Institute of Microelectronics, Agency for Science, Technology and Research (A\*STAR), 138634 Singapore, Singapore. <sup>10</sup>School of Physics and Microelectronics, Zhengzhou University, Zhengzhou 450052, China. <sup>11</sup>These authors contributed equally: Shu Shi, Haolong Xi, Tengfei Cao, Weinan Lin. ✉ e-mail: [yanxiaobing@ime.ac.cn](mailto:yanxiaobing@ime.ac.cn); [tsybal@unl.edu](mailto:tsybal@unl.edu); [hetian@zju.edu.cn](mailto:hetian@zju.edu.cn); [msecj@nus.edu.sg](mailto:msecj@nus.edu.sg)

which transforms into the tetragonal phase ( $P4_2/nmc$ ) at 2773 K and then to the monoclinic phase ( $P2_1/c$ ) at 1937 K upon cooling<sup>15</sup>. However, the crystal structures of these polymorphs of  $\text{HfO}_2$  are non-ferroelectric. It has been recognized that the ferroelectricity in  $\text{HfO}_2$ -based materials is related to the low symmetry orthorhombic phase ( $Pca2_1$ )<sup>16</sup>, which can be stabilized with the help of thin-film growth<sup>17–20</sup>. Therefore, the rational engineering capability of the thin-film growth becomes critical for achieving robust ferroelectricity in  $\text{HfO}_2$ -based materials.

$\text{Hf}_{0.5}\text{Zr}_{0.5}\text{O}_2$  (HZO) has the most robust ferroelectric properties among the reported doped-hafnium oxides<sup>4,21–32</sup>. However, up to date, most of the HZO thin films studied were polycrystalline, which contained secondary non-ferroelectric phases that suppressed the ferroelectric properties and obscured the understanding of the fundamental physics of ferroelectric HZO<sup>17,33,34</sup>. It was demonstrated that the ferroelectric orthorhombic phase can be stabilized in epitaxial HZO films grown on a perovskite substrate<sup>35–41</sup>. Notably, it was found that the  $\text{La}_{0.67}\text{Sr}_{0.33}\text{MnO}_3$  (LSMO) buffer layer is essential in the epitaxial growth of ferroelectric HZO<sup>18,19,36,42</sup>. Given that fluorite-like HZO and perovskite LSMO have different structures, there is a lattice mismatch between them. A few mechanisms for obtaining the ferroelectric phase of HZO by the LSMO buffer layer have been proposed, such as the interface reconstruction<sup>18</sup> and the domain matching epitaxy<sup>43</sup>. Recently, ref. 44 reported that chemical reconstruction at the HZO/LSMO interface, where the substitution of the Mn cations by Hf or Zr cations occurs during the epitaxial growth of HZO on LSMO. However, the role of LSMO in the stabilization of the ferroelectric *o*-phase is still unclear, and its physical mechanism is not well understood.

In this work, we demonstrate the enhanced stabilization of the ferroelectric *o*-phase in HZO by the deliberate control of the termination of the bottom LSMO layer, namely, the  $\text{MnO}_2$  termination or the LaSrO termination. We find that HZO films grown on the  $\text{MnO}_2$ -terminated LSMO exhibit a more enhanced ferroelectric phase than those grown on the LaSrO-terminated LSMO. We provide a useful strategy to stabilize the ferroelectric phase in ultrathin HZO films<sup>45,46</sup>. Even though the HZO layer is as thin as 1.5 nm, the clear ferroelectric orthorhombic (111) crystal orientation is observed on the  $\text{MnO}_2$ -terminated LSMO. Based on scanning transmission electron microscopy (STEM) measurements and density functional theory (DFT) calculations, we argue that hole doping of HZO resulting from the electrostatic potential difference at the interface is the origin of the enhanced fraction of the ferroelectric *o*-phase of HZO.

## Results

### Interface engineering of epitaxial HZO films

We utilize the state-of-the-art growth technique<sup>47</sup> to rationally fabricate two types of HZO/LSMO structures, which are different by the interface termination of LSMO: one has the  $\text{MnO}_2$  termination (A-type) and the other has the LaSrO termination (B-type), as schematically shown in Fig. 1a, b. The HZO/ $\text{MnO}_2$  terminated structure is obtained by growing LSMO layer-by-layer on top of the treated  $\text{SrTiO}_3$  substrate with  $\text{TiO}_2$  termination, while the HZO/LaSrO-terminated structure is obtained by inserting a  $\text{SrRuO}_3$  layer between LSMO and treated  $\text{SrTiO}_3$  substrate, where the volatile  $\text{RuO}_2$  is evaporated at the elevated temperature and SrO termination is remained (see the “Methods” section for the detailed growth strategy). The film thickness and the interfacial termination are precisely controlled with the help of

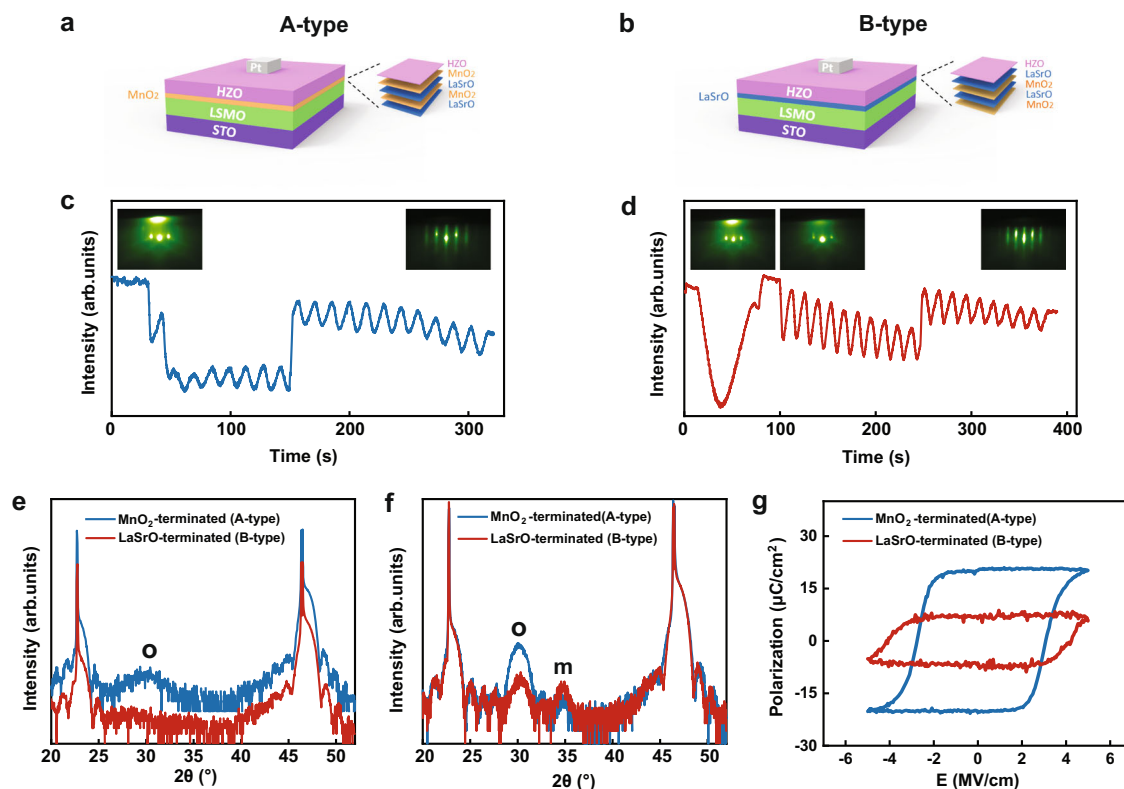


**Fig. 1 | RHEED, XRD characterization, and ferroelectric characterization of A- and B-type HZO/LSMO heterostructures.** **a, b** Schematic of the A-type (HZO/ $\text{MnO}_2$ ) terminated and B-type (HZO/LaSrO) terminated structure. The atomic plane sequences across the HZO/LSMO interfaces are indicated. **c, d** RHEED intensity oscillations of the specularly reflected beam during the growth of A- and B-type structure. The insets indicate the RHEED patterns before and after the growth of

each layer. **e, f**  $\omega$ - $2\theta$  scan of XRD characterization for A-type and B-type heterostructures with HZO thickness of (e) 1.5 nm and (f) 8 nm. “o” indicates the orthorhombic phase HZO and “m” indicates the monoclinic phase HZO. **g** Positive-up-negative-down (PUND) polarization-electric field loops for the A-type (blue) and B-type (red) heterostructures. The HZO layer thickness is  $t_{\text{HZO}} = 8$  nm.

reflection high-energy electron diffraction (RHEED) monitoring (Fig. 1c, d). The x-ray reflectivity measurements, as shown in Supplementary Fig. S1, further confirm the smooth interface and the thickness of HZO films. Figure 1e, f show the crystallographic information of these two types of heterostructures (with HZO thickness of 1.5 and 8 nm, respectively) obtained by XRD measurements. It is seen that in both structures, a characteristic peak at about  $30^\circ$  is observed at the HZO thickness of 8 nm, which represents the orthorhombic phase HZO (*o*-HZO (111)). Another characteristic peak located at about  $35^\circ$  in the measured XRD data represents the monoclinic phase of HZO (*m*-HZO (002)). The coexistence of the *o*- and *m*-phases is common for the epitaxial HZO films, and generally, the fraction ratio of the *o*-phase to *m*-phase decreases with the increase of the HZO film thickness<sup>35</sup>. Notably, we find that the XRD peak of ferroelectric *o*-phase HZO in the A-type heterostructure is stronger than that in the B-type heterostructure, while the peak of non-ferroelectric *m*-phase HZO is less pronounced, indicating that the A-type heterostructure contains a greater fraction of the ferroelectric *o*-phase HZO component. Moreover, for an HZO thickness of 1.5 nm, *o*-HZO (111) can only be observed on the HZO/MnO<sub>2</sub> terminated sample. This is consistent with the previous report, where the *o*-HZO (111) phase was also not formed on the mixed termination of the LSMO buffer layer (untreated LSMO)<sup>18</sup>. This result indicates that with the MnO<sub>2</sub> terminated buffer layer, the fundamental limits of ferroelectric HZO *o*-phase can be enhanced and pushed to below 1.5 nm. The enhancement of the ferroelectric *o*-phase on MnO<sub>2</sub> termination is consistently observed when the HZO layer thicknesses are 3 and 5 nm (Supplementary Fig. S2).

### Ferroelectric properties of HZO films with different terminations of LSMO

Ferroelectric polarization-electric field loops (P-E loops) for A- and B-type heterostructures allow characterizing the ferroelectric polarization quantitatively. These measurements are performed using HZO films with deposited Pt top electrode films. As seen from Fig. 1g, the A-type heterostructure (with an HZO thickness of 8 nm) has a higher remnant polarization value than that of the B-type heterostructure. This result is in line with our XRD and STEM characterizations, suggesting that the A-type heterostructure favors the formation of ferroelectric *o*-phase HZO and therefore yields a higher  $P_r$ . Additionally, to further examine the ferroelectricity in our ultrathin HZO film, the in-plane P-E loop measurement for the A-type heterostructure sample (with an HZO thickness of 1.5 nm) is performed (Supplementary Fig. S3). The bistable current-voltage loops (Supplementary Fig. S4) show clear switching current and non-leaky characteristics of our heterostructures. It is interesting to note that the A-type heterostructure shows steady P-E loops upon cycling (Supplementary Fig. S5a), without the widely observed wake-up cycling required for other hafnia-based systems<sup>21</sup>, while the B-type heterostructure shows obvious wake-up behavior in the first 1000 cycles (Supplementary Fig. S5b). Generally, the diffusion and redistribution of oxygen vacancies is believed to account for the wake-up effect<sup>21,48–51</sup>. Our results suggest that the wake-up may be attributed to the existence of the non-ferroelectric phase in the films. The interfacial engineering strategy can effectively stabilize the ferroelectric *o*-phase and thus avoid the wake-up behavior in HZO film. In addition, we performed an endurance test for the HZO films, and remarkably, the sample with A-type heterostructure did not break down after  $10^9$  cycles using the same poling voltage (Supplementary Fig. S5c). Our result shows a high-level endurance of the epitaxial HZO films grown by the interface engineering strategy<sup>52,53</sup>. Lyu et al.<sup>54</sup> reported an endurance of over  $10^{11}$  cycles for epitaxial HZO films with a wake-up effect. For those epitaxial HZO films without wake-up cycling, the endurance is generally lower than  $10^6$  (ref. <sup>18</sup>).

The ferroelectric switching behavior of the HZO films with two heterostructures are studied by the piezo-response force microscopy

(PFM) technique. The ferroelectric domain switching of the HZO films with a film thickness of 8 and 1.5 nm is demonstrated by applying the positive and negative poling voltages to them (see Supplementary Figs. S6–8). Our result shows good retention of ferroelectric switching of 8 nm HZO samples with two types of heterostructures (Supplementary Fig. S7b, f). The retention of ferroelectric switching of A-type heterostructure with an HZO thickness of 1.5 nm is shown in Supplementary Fig. S8e. However, a clear ferroelectric switching PFM contrast is very difficult to obtain in the B-type heterostructure with an HZO thickness of 1.5 nm (Supplementary Fig. S8c), which is in line with our XRD data (Fig. 1e) that no ferroelectric *o*-phase is observed in this sample.

### Stabilization of ferroelectric *o*-phase and interface reconstruction

STEM and electron energy-loss spectroscopy (EELS) characterization are performed to further provide insights into the structural properties of the two heterostructures. Figure 2a, b show high-angle annular dark field (HAADF) images and atomic-resolution energy-dispersive x-ray (EDX) elemental maps of the cross-section of the A- and B-type heterostructures. The bottom LSMO layer has a perfect epitaxial (001) relationship with a slightly compressed c-axis with respect to the STO substrate. The phase identification in the two heterostructures is performed by analyzing the atomic structure in HAADF-STEM images and combining with Fast Fourier Transform (FFT) (Supplementary Fig. S9). At the same time, the HZO demonstrates a highly textured growth on the bottom LSMO layer. We find that in the A-type heterostructure, the majority phase of HZO is the ferroelectric *o*-phase, while the minority phase is the non-ferroelectric *m*-phase (Fig. 2a, also see Supplementary Fig. S10). On the contrary, in the B-type heterostructure, the *m*-phase has a larger fraction compared to the A-type heterostructure (Fig. 2b). Statistics analysis of *m*-phase and *o*-phase crystalline grains helps to quantify the *m*-phase and the *o*-phase distribution in two heterostructures (see Supplementary Fig. S11). This microscopic observation by STEM is consistent with the macroscopic XRD results of the two types of structures. However, as is evident from the EDX elemental maps (Fig. 2a, b, right panels), the terminations of the LSMO layers in the A- and B-type heterostructures appear to be similar, both exhibiting a stronger LaSrO EDX contrast at the atomic plane terminating LSMO. This is unexpected for the precise layer-by-layer growth mode designed for the two types of structures. The difference between the A- and B-type interface structures occurs in the HZO layer regions adjacent to the interface. Our out-of-plane spacing analysis (Fig. 3) provides evidence for the interface reconstruction in the A-type heterostructures. Figure 3c shows the spacing between atomic layers for the A-type sample. It is seen that the HZO atomic layer spacing at the interface region is about 0.34 nm, which is much larger than that away from the interface (about 0.26 nm). For the B-type sample, the HZO atomic layer spacing at the interface is about 0.26 nm (Fig. 3d), basically the same as the spacing at the *m*-HZO/LSMO interface region. This difference indicates that an interface reconstruction occurs in the A-type HZO/LSMO heterostructure. A similar result was obtained by Estandía et al.<sup>42</sup>, who argued that the HZO/LSMO interface reconstruction is associated with partial substitution of the interfacial Mn atoms with Hf (Zr). This result can be understood in terms of the polar nature of the pristine MnO<sub>2</sub>-terminated LSMO surface and the nominal ionic charges of Hf and Mn cations. Due to a higher ionic charge of Hf<sup>4+</sup> compared to Mn<sup>3,33</sup> in LSMO, the substitution of Hf for Mn is energetically favorable due to the reduced polarity of the interface<sup>42</sup>. A similar phenomenon was also reported for LaFeO<sub>3</sub>/n-SrTiO<sub>3</sub> heterostructures<sup>55</sup>.

### Charge transfer at the LSMO/HZO interface

In addition to the interface reconstruction, we observe an effect of charge transfer at the LSMO/HZO interface evident from our

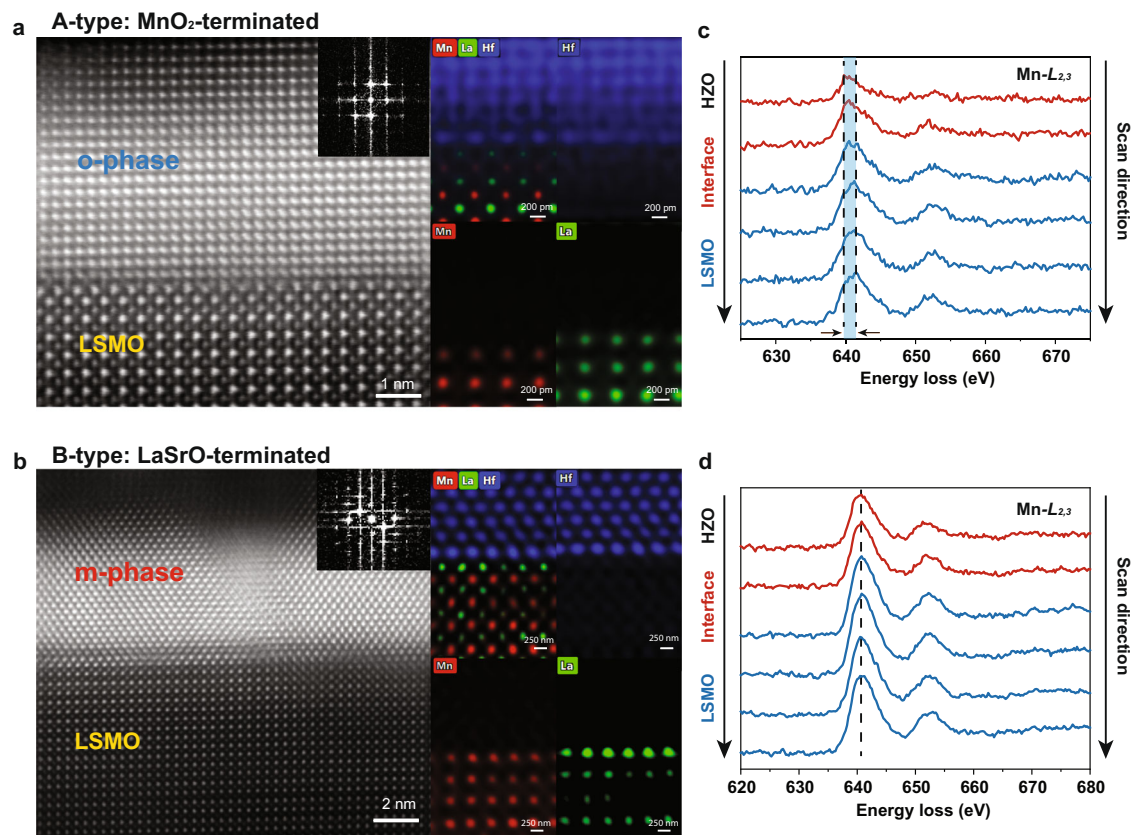


**Fig. 2 | HAADF-STEM characterization.** **a** Cross-section image and atomically resolved EDX for A-type heterostructure. **b** Cross-section image and atomically resolved EDX for B-type heterostructure, which are observed along the [110] zone of the substrate. Mn, La, and Hf atoms in the EDX maps are seen in red, green, and

blue colors, respectively. **c, d** Layer-resolved EELS spectra of Mn- $L_{2,3}$  edge for **c** A-type and **d** B-type heterostructures. Arrows indicate the scan direction. Dashed lines mark the Mn- $L_{2,3}$  peak positions. The blue area between the dashed lines indicates the energy loss shift of the Mn-L edge.

atomically resolved EELS data (Fig. 2c, d). For the A-type heterostructure, we detect an energy loss shift of about 1.25 eV of the Mn-L edge from the bottom to the top across the interface (Fig. 2c), indicating a decrease in the Mn valence<sup>56</sup>. In contrast, no such energy shift of the Mn-L edge is observed for the B-type heterostructure (Fig. 2d). Combined with the structural characterization results (Fig. 1), our EELS analysis suggests an important role of the charge transfer in the stabilization of the ferroelectric phase in HZO thin films<sup>57</sup>.

To further support this inference, we fabricated two control samples with a 2-unit-cell  $\text{LaMnO}_3$  layer inserted between HZO and LSMO layers in both A- and B-type heterostructures (see “Methods”). The motivation for this test was the control of the interface ionic charge and, thus, interface charge transfer between the LSMO and HZO layers in the heterostructures. A pristine  $\text{La}_{0.67}\text{Sr}_{0.33}\text{MnO}_3$  (001) surface with  $\text{MnO}_2$ -termination has a net charge of  $-0.67$ , while that surface with the  $\text{LaSrO}$ -termination has a charge of  $+0.67$ . On the contrary, the structure with the inserted  $\text{LaMnO}_3$  leads to  $\text{MnO}_2^{(-)}$ -termination with a negative charge and  $\text{LaO}^{(+)}$ -termination with a positive charge (Fig. 4a), for A- and B-type heterostructures, respectively. We found that the  $\text{MnO}_2^{(-)}$ -terminated structure shows strong peaks of both *o*-phase and *m*-phase HZO, while the  $\text{LaO}^{(+)}$ -terminated structure only shows a strong peak of *m*-phase HZO (Fig. 4b). This observation indicates that a negative ionic charge of the  $\text{MnO}_2$ -termination plays a key role in the formation of *o*-phase in the HZO film, while a positive charge of the  $\text{LaO}$ -termination may hinder the formation of the *o*-phase in HZO or facilitate the *m*-phase in HZO. Our control experiment strongly supports the important role of the charge transfer at the LSMO/HZO interface in the stabilization of the *o*-phase in the HZO films.

### Hole doping mechanism for stabilization of ferroelectric *o*-phase

The importance of the charge transfer in the stabilization of the ferroelectric *o*-phase is confirmed by our DFT calculations (see “Methods” for details). The appearance of the charge transfer is qualitatively inferred from the comparison of the calculated work functions of HZO and LSMO with A- and B-type surface terminations. As shown in Fig. 4c, the work function of *o*-HZO (defined as the energy difference between the vacuum level and the valence band maximum) is calculated to be 3.45 eV. The work functions of the  $\text{LaO}$ -,  $\text{LaSrO}$ -, and  $\text{MnO}_2$ -terminated LSMO are calculated to be 1.25, 1.70, and 5.94 eV, respectively. These differences in the work functions demonstrate that during the epitaxial growth of *o*-HZO films on LSMO, there is charge transfer between the *o*-HZO and LSMO layers. Due to the larger work function of the  $\text{MnO}_2$ -terminated LSMO (5.94 eV) compared to *o*-HZO (3.45 eV), the  $\text{MnO}_2$ -terminated LSMO is expected to attract electrons from HZO and become negatively charged during epitaxial growth of HZO. This is consistent with our experimental observations of the reduced valence of the Mn ions at the  $\text{MnO}_2$ -terminated interface. Therefore, HZO films grown on  $\text{MnO}_2$ -terminated LSMO are under electron-deficient (or hole-rich) conditions. These conditions are supportive of the ferroelectric *o*-phase of HZO, as found in our experiments. In contrast, HZO films grown on  $\text{LaO}$ - and  $\text{LaSrO}$ -terminated LSMO are under electron-rich conditions, where the non-ferroelectric *m*-phase is the dominant structural phase of HZO detected in our experiments. To further prove that hole doping could stabilize the ferroelectric phase of HZO, we calculate the energy difference between *o*-HZO and *m*-HZO phases for different levels of doping. The results are displayed in Fig. 4d. It is seen that the *m*-phase of HZO is energetically more favorable than the *o*-phase at zero doping. Hole doping gradually reduces the energy

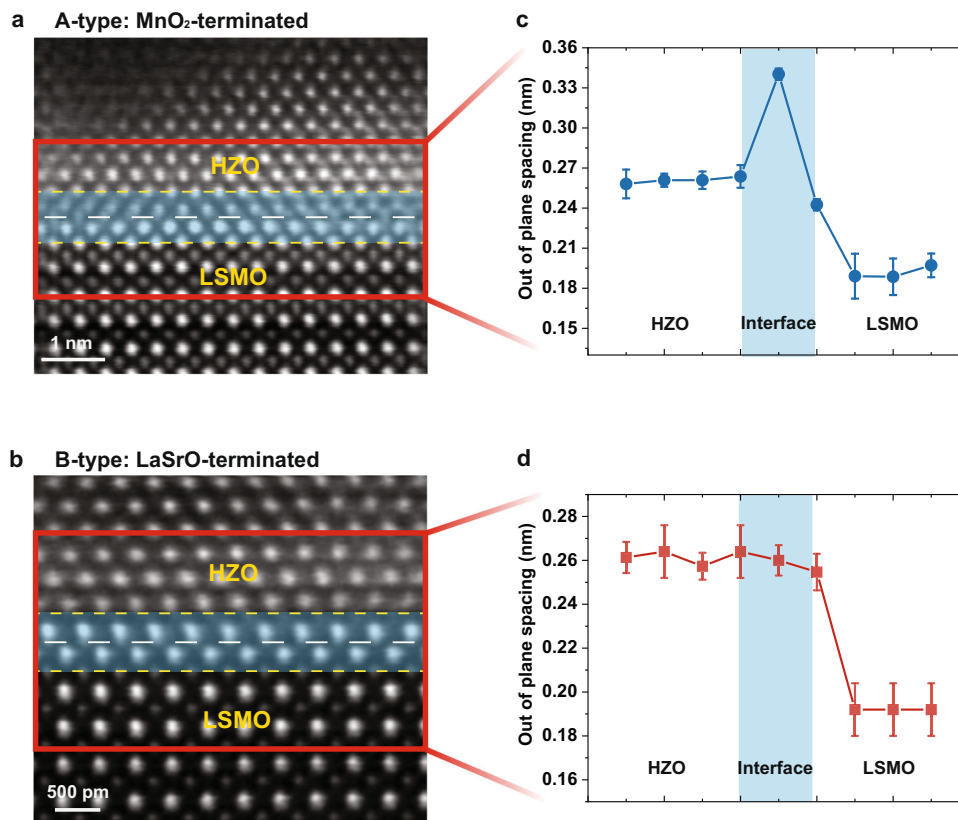


**Fig. 3 | HAADF-STEM images and out-of-plane analysis.** **a, b** Cross-section images of A- and B-type heterostructures. The white dashed lines indicate the interfaces between HZO and LSMO. **c, d** Out-of-plane spacing within the red-frame region in A- and B-type heterostructure samples. The regions confined by the

yellow dotted lines in **(a, b)** correspond to the blue color regions in **(c, d)**. Error bars are calculated from the out-of-plane measurements of different regions for each sample.

difference between *o*-HZO and *m*-HZO phases. Therefore, hole doping is favorable for stabilizing the *o*-HZO phase. When the hole concentration becomes larger than 0.17 h/u.c., the *o*-HZO phase becomes the ground state. Electron doping, on the other hand, is detrimental to the stabilization of the *o*-HZO phase.

## Discussion

All the above results clearly show that extra holes contribute to stabilizing the ferroelectric phase of HZO, and the stabilization effect is determined by the amount of charge exchange between the HZO film and the substrate. This is also consistent with our experimental observations on different substrates. During the synthesis process, we adopted both LSMO and LMO buffer layers to achieve the ferroelectric phase of HZO films. For both LaO-terminated LMO and LSMO (or LaO-termination), we can only grow the nonpolar *m*-HZO phase, because LaO-termination donates electrons to HZO, which can only facilitate the growth of *m*-HZO (Fig. 4b). For MnO<sub>2</sub>-terminated substrates; however, there are differences in final growth phases of HZO films. We achieve almost pure *o*-HZO films on the MnO<sub>2</sub>-terminated LSMO, but we can only synthesize mixed *o*- and *m*-HZO phases on the MnO<sub>2</sub>-terminated LMO. These differences could also be understood from surface work functions and involved charge exchanges during the synthesis process. For MnO<sub>2</sub>-terminated LSMO and LMO, their surface work functions are calculated to be 5.94 and 4.79 eV, respectively. Considering the surface work function of HZO is 3.79 eV, there will be more holes transferred to HZO films grown on LSMO than those grown on LMO. Therefore, the *o*-HZO phase is more favorable on the MnO<sub>2</sub>-terminated LSMO than that on LMO.

In summary, we have demonstrated an enhanced ferroelectric *o*-phase in HZO thin films by engineering the termination of the HZO/

LSMO interface. Such interface engineering permits stabilization of the metastable ferroelectric *o*-phase in epitaxial HZO thin films, which originates from hole doping from the MnO<sub>2</sub>-terminated LSMO to the HZO layer. The insights gained in this work establish a critical role of the LSMO termination layer in stabilizing the ferroelectric phase in HZO thin films and provide a clue for understanding ferroelectricity in hafnia-based films. This work also suggests a strategy to generate enhanced ferroelectric polarization in HZO thin films. We hope that our results will inspire further exploration of interface engineering to enhance ferroelectricity in hafnia-based systems.

## Methods

### Thin film deposition

Ferroelectric HZO films on La<sub>0.67</sub>Sr<sub>0.33</sub>MnO<sub>3</sub> (LSMO) bottom electrodes were epitaxially grown on single-crystalline STO (001) substrates by pulsed laser deposition (PLD) using a KrF ( $\lambda = 248$  nm) excimer laser. The bottom HZO/LSMO interface was fabricated either HZO/MnO<sub>2</sub> or HZO/La<sub>0.67</sub>Sr<sub>0.33</sub>O terminated. LSMO thin films (20 u.c.) were grown at a substrate temperature of 950 °C with an oxygen pressure of 200 mTorr, while HZO films (1.5–8 nm) were deposited at a temperature of 800 °C with an oxygen pressure of 75 mTorr. The laser fluence was 1.25 J cm<sup>-2</sup> with a repetition rate of 3 Hz. LSMO thin films were deposited with the layer-by-layer growth mode monitored by RHEED oscillations. In order to control the interface termination, STO substrates were treated with a buffered hydrofluoric acid etching process followed by thermal treatment at 875 °C for 3 h to get a TiO<sub>2</sub>-terminated surface before growth. The SrO-terminated surface was obtained by the growth of 1 u.c. of SrRuO<sub>3</sub> (SRO) layer on top of treated STO substrates. The SRO thin layer was deposited at a temperature of 950 °C with an oxygen

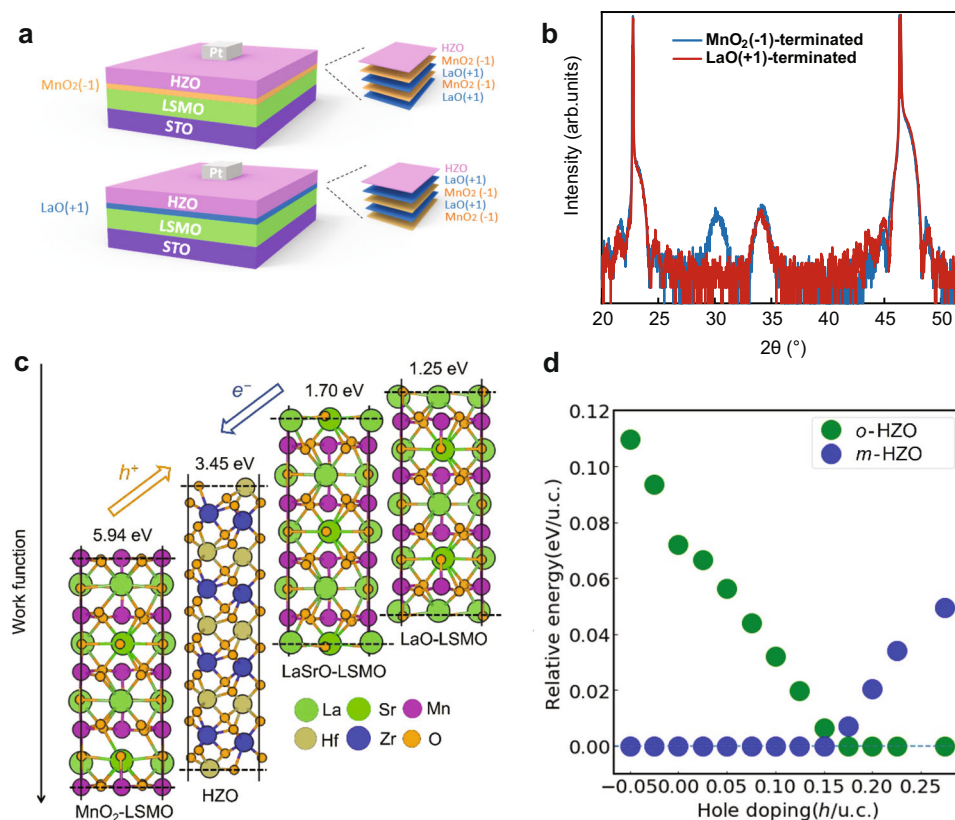


**Fig. 4 | Interface charge tuning and theoretical results.** **a** Schematic of the  $\text{MnO}_2^{(-1)}$ -terminated structure (top) and  $\text{LaO}^{(+1)}$ -terminated structure (bottom) obtained by inserting a 2-unit-cell  $\text{LaMnO}_3$  layer between HZO and LSMO layers. The resulting termination is  $\text{MnO}_2^{(-1)}$  with a negative ionic charge or  $\text{LaO}^{(+1)}$  with a positive ionic charge for A- and B-type heterostructures, respectively. **b** XRD data for the  $\text{MnO}_2^{(-1)}$ -terminated structure (blue curve) and the  $\text{LaO}^{(+1)}$ -terminated structure (red curve). **c** Calculated work functions of *o*-HZO,  $\text{MnO}_2$ -terminated

LSMO ( $\text{MnO}_2$ -LSMO),  $\text{LaSrO}$ -terminated LSMO ( $\text{LaSrO-LSMO}$ ), and  $\text{LaO}$ -terminated LSMO ( $\text{LaO-LSMO}$ ).  $\text{MnO}_2$ -terminated LSMO donates holes to HZO, while  $\text{LaSrO}$ - and  $\text{LaO}$ -terminated LSMO donates electrons. **d** Relative stability of orthorhombic (green circles) and monoclinic (blue circles)  $\text{HfO}_2$  phases as a function of hole doping density. The lowest energy phase is used as the reference, and its energy is set to zero. The energy of the other phase is given with respect to the most stable one.

pressure of 5 mTorr and then left at 950 °C for 10 min. The laser fluence was  $1.1 \text{ J cm}^{-2}$  with a repetition rate of 1 Hz. At a high temperature, the  $\text{RuO}_2$  monolayer of SRO evaporated, leaving the SrO-terminated surface automatically. Control samples were fabricated using a 2-unit cell of  $\text{LaMnO}_3$  layer deposited between the HZO and LSMO layers to tune the charge state of the termination. Since  $\text{LaMnO}_3$  exhibits a  $\text{MnO}_2$ - $\text{LaO}$ - $\text{MnO}_2$ - $\text{LaO}$  layer-by-layer growth mode during the PLD process, deposition of a 2-u.c.  $\text{LaMnO}_3$  at the interface results in either  $\text{MnO}_2$ -termination with a negative charge of  $-1$  or  $\text{LaO}$ -termination with a positive charge of  $+1$ . After the deposition, the films were cooled down to room temperature at an oxygen pressure of 1 torr with a cooling rate of 10 °C/min. The top Pt layer was deposited by magnetron sputtering without breaking the vacuum by transferring the sample from the PLD system into the sputtering system for in situ growth. Then, an array of  $10 \times 10 \mu\text{m}^2$  top Pt electrodes was patterned via photolithography and ion etching for electrical measurements.

### Ferroelectricity measurements

The ferroelectric measurements (P-E hysteresis loops) were performed using a Radiant Precision Multiferroic II tester. Ferroelectric polarization and local hysteresis loops of HZO thin films were characterized by piezoelectric force microscopy (PFM) using an Asylum Research MFP-3D instrument with Pt/Ti-coated tips. A 30 nm of Pt with a device feature of  $10 \times 10 \mu\text{m}^2$  was sputtered as the top electrode material prior to the ferroelectric test. For the out-of-plane P-E measurement, a bipolar triangular waveform was applied at frequencies  $\sim 100$  kHz. For

the in-plane P-E measurement, a bipolar triangular waveform was applied at frequencies  $\sim 20$  kHz, with the interdigitated electrode spacing of around  $5 \mu\text{m}$ .

### Material characterization

Microstructure of the samples, interfacial structure, EDX elemental mapping, and atomic layer-by-layer EELS were obtained by aberration-corrected STEM at room temperature. Cross-sectional TEM samples were prepared with a focused ion beam setup (DA300, FEI). The crystal structure and epitaxial quality were characterized by synchrotron XRD using a four-circle diffractometer with an X-ray wavelength of  $1.5406 \text{ \AA}$  at the Singapore Synchrotron Light Source.

### Theoretical modeling and DFT calculations

Density functional theory (DFT) calculations were performed using the Vienna Ab-initio Simulation Package (VASP)<sup>58</sup>. Projector augmented-wave (PAW) potentials and the generalized gradient approximation (GGA) within the Perdew–Burke–Ernzerhof (PBE) parameterization were used to describe the electron-ion and the electronic exchange-correlation interactions<sup>59,60</sup>. The energy cut-off for the plane waves was set at 500 eV. The threshold for the energy convergence of the self-consistent loops was set at  $10^{-6}$  eV. For structural optimization, the convergence of forces was set to be  $10^{-3} \text{ eV \AA}^{-1}$ . The slab model was used to calculate the work functions of HZO,  $\text{MnO}_2$ ,  $\text{LaO}$ , and  $\text{LaSrO}$ -terminated LSMO. We built the HZO slab from the orthorhombic ferroelectric bulk phase of  $\text{HfO}_2$ , where half of the Hf atoms is substituted with Zr, along the nonpolar (100) direction, to eliminate the electric

field in vacuum. Figure 4a shows the slab structure, which has the in-plane lattice of  $5.073 \text{ \AA} \times 5.098 \text{ \AA}$ , contains 8 Hf, 8 Zr, and 12 O atoms, and has a  $15 \text{ \AA}$  vacuum layer to exclude interaction between the slab and its periodic images. For  $\text{MnO}_2$ -,  $\text{LaO}$ -, and  $\text{LaSrO}$ -terminated LSMO models, to simplify the calculations, we assumed the LSMO stoichiometry to be represented by  $\text{La}_{0.75}\text{Sr}_{0.25}\text{MnO}_3$  and  $\text{LaSrO}$ -termination to be  $\text{La}_{0.5}\text{Sr}_{0.5}\text{O}$ . We cut the slabs from the ferromagnetic  $\text{LaMnO}_3$  bulk phase (space group of  $Pnma$ ) along the (001) direction, and substituted a quarter of La atoms with Sr. The LSMO slabs of different terminations are shown in Fig. 4a. For all these slabs, in plan lattices of  $5.526 \text{ \AA} \times 5.544 \text{ \AA}$  and  $15 \text{ \AA}$  vacuum layer are applied, and ferromagnetic order is utilized. Our calculations show that the work function difference between  $\sigma$ -HZO and LSMO is relatively large. Therefore, even though the work function of  $\text{La}_{0.67}\text{Sr}_{0.33}\text{MnO}_3$  may be slightly different from that of  $\text{La}_{0.75}\text{Sr}_{0.25}\text{MnO}_3$ , the main trend found here will not change. To simulate charge doping effects on the phase stability of HZO, an electronic charge of a certain density was added (electron doping) or removed (hole doping) to bulk HZO on a charge-neutralizing positive or negative background. Then the corresponding structures were fully optimized, and the total energies of  $\sigma$ - and  $m$ -phases were calculated.

### Reporting summary

Further information on research design is available in the Nature Portfolio Reporting Summary linked to this article.

### Data availability

The data that support the findings of this study are available from the corresponding author upon reasonable request. Source data are provided with this paper.

### References

- Böscke, T. S., Müller, J., Bräuhäus, D., Schröder, U. & Böttger, U. Ferroelectricity in hafnium oxide thin films. *Appl. Phys. Lett.* **99**, 102903 (2011).
- Chernikova, A. et al. Ultrathin  $\text{Hf}_{0.5}\text{Zr}_{0.5}\text{O}_2$  ferroelectric films on Si. *ACS Appl. Mater. Interfaces* **8**, 7232–7237 (2016).
- Lee, H.-J. et al. Scale-free ferroelectricity induced by flat phonon bands in  $\text{HfO}_2$ . *Science* **369**, 1343–1347 (2020).
- Cheema, S. S. et al. Enhanced ferroelectricity in ultrathin films grown directly on silicon. *Nature* **580**, 478–482 (2020).
- Cheema, S. S. et al. Ultrathin ferroic  $\text{HfO}_2$ - $\text{ZrO}_2$  superlattice gate stack for advanced transistors. *Nature* **604**, 65–71 (2022).
- Florent, K. et al. Vertical ferroelectric  $\text{HfO}_2$  FET based on 3-D NAND architecture: towards dense low-power memory. In *2018 IEEE International Electron Devices Meeting (IEDM)* 2.5.1–2.5.4 (IEEE, 2018).
- Zeng, B. et al. 2-Bit/cell operation of  $\text{Hf}_{0.5}\text{Zr}_{0.5}\text{O}_2$  based FeFET memory devices for NAND applications. *IEEE J. Electron Devices Soc.* **7**, 551–556 (2019).
- Ali, T. et al. Silicon doped hafnium oxide (HSO) and hafnium zirconium oxide (HZO) based FeFET: a material relation to device physics. *Appl. Phys. Lett.* **112**, 222903 (2018).
- Park, M. H., Lee, Y. H., Mikolajick, T., Schroeder, U. & Hwang, C. S. Review and perspective on ferroelectric  $\text{HfO}_2$ -based thin films for memory applications. *MRS Commun.* **8**, 795–808 (2018).
- Schroeder, U. et al. Hafnium oxide based CMOS compatible ferroelectric materials. *ECS J. Solid State Sci. Technol.* **2**, N69–N72 (2013).
- Kim, M.-K. & Lee, J.-S. Ferroelectric analog synaptic transistors. *Nano Lett.* **19**, 2044–2050 (2019).
- Böscke, T. S., Müller, J., Bräuhäus, D., Schröder, U. & Böttger, U. Ferroelectricity in hafnium oxide: CMOS compatible ferroelectric field effect transistors. In *2011 International Electron Devices Meeting* 24.5.1–24.5.4 (IEEE, 2011).
- Müller, J. et al. Ferroelectricity in  $\text{HfO}_2$  enables nonvolatile data storage in 28 nm HKMG. In *2012 Symposium on VLSI Technology (VLSIT)* 25–26 (IEEE, 2012).
- Chouprik, A., Negrov, D., Tsybmal, E. Y. & Zenkevich, A. Defects in ferroelectric  $\text{HfO}_2$ . *Nanoscale* **13**, 11635–11678 (2021).
- Schroeder, U. et al. Recent progress for obtaining the ferroelectric phase in hafnium oxide based films: impact of oxygen and zirconium. *Jpn. J. Appl. Phys.* **58**, SL0801 (2019).
- Sang, X., Grimley, E. D., Schenk, T., Schroeder, U. & LeBeau, J. M. On the structural origins of ferroelectricity in  $\text{HfO}_2$  thin films. *Appl. Phys. Lett.* **106**, 162905 (2015).
- Park, M. H. et al. Ferroelectricity and antiferroelectricity of doped thin  $\text{HfO}_2$ -based films. *Adv. Mater.* **27**, 1811–1831 (2015).
- Wei, Y. et al. A rhombohedral ferroelectric phase in epitaxially strained  $\text{Hf}_{0.5}\text{Zr}_{0.5}\text{O}_2$  thin films. *Nat. Mater.* **17**, 1095–1100 (2018).
- Yun, Y. et al. Intrinsic ferroelectricity in Y-doped  $\text{HfO}_2$  thin films. *Nat. Mater.* **21**, 903–909 (2022).
- Kang, S. et al. Highly enhanced ferroelectricity in  $\text{HfO}_2$ -based ferroelectric thin film by light ion bombardment. *Science* **376**, 731–738 (2022).
- Xu, X. et al. Kinetically stabilized ferroelectricity in bulk single-crystalline  $\text{HfO}_2$ :Y. *Nat. Mater.* **20**, 826–832 (2021).
- Fan, Z. et al. Ferroelectricity emerging in strained (111)-textured  $\text{ZrO}_2$  thin films. *Appl. Phys. Lett.* **108**, 012906 (2016).
- Müller, J. et al. Ferroelectricity in simple binary  $\text{ZrO}_2$  and  $\text{HfO}_2$ . *Nano Lett.* **12**, 4318–4323 (2012).
- Böscke, T. S. et al. Phase transitions in ferroelectric silicon doped hafnium oxide. *Appl. Phys. Lett.* **99**, 112904 (2011).
- Mueller, S. et al. Incipient ferroelectricity in Al-doped  $\text{HfO}_2$  thin films. *Adv. Funct. Mater.* **22**, 2412–2417 (2012).
- Mimura, T., Shimizu, T., Uchida, H., Sakata, O. & Funakubo, H. Thickness-dependent crystal structure and electric properties of epitaxial ferroelectric  $\text{Y}_2\text{O}_3$ - $\text{HfO}_2$  films. *Appl. Phys. Lett.* **113**, 102901 (2018).
- Lee, Y. H. et al. Preparation and characterization of ferroelectric  $\text{Hf}_{0.5}\text{Zr}_{0.5}\text{O}_2$  thin films grown by reactive sputtering. *Nanotechnology* **28**, 305703 (2017).
- Song, T. et al. Epitaxial ferroelectric La-doped  $\text{Hf}_{0.5}\text{Zr}_{0.5}\text{O}_2$  thin films. *ACS Appl. Electron. Mater.* **2**, 3221–3232 (2020).
- Schenk, T. et al. On the origin of the large remanent polarization in La: $\text{HfO}_2$ . *Adv. Electron. Mater.* **5**, 1900303 (2019).
- Hoffmann, M. et al. Stabilizing the ferroelectric phase in doped hafnium oxide. *J. Appl. Phys.* **118**, 072006 (2015).
- Shiraishi, T. et al. Fabrication of ferroelectric Fe doped  $\text{HfO}_2$  epitaxial thin films by ion-beam sputtering method and their characterization. *Jpn. J. Appl. Phys.* **57**, 11UF02 (2018).
- Cao, J., Shi, S., Zhu, Y. & Chen, J. An overview of ferroelectric hafnia and epitaxial growth. *Phys. Status Solidi Rapid Res. Lett.* **15**, 2100025 (2021).
- Nukala, P. et al. Reversible oxygen migration and phase transitions in hafnia-based ferroelectric devices. *Science* **372**, 630–635 (2021).
- Park, M. H. et al. Understanding the formation of the metastable ferroelectric phase in hafnia-zirconia solid solution thin films. *Nanoscale* **10**, 716–725 (2018).
- Lyu, J., Fina, I., Solanas, R., Fontcuberta, J. & Sánchez, F. Growth window of ferroelectric epitaxial  $\text{Hf}_{0.5}\text{Zr}_{0.5}\text{O}_2$  thin films. *ACS Appl. Electron. Mater.* **1**, 220–228 (2019).
- Yoong, H. Y. et al. Epitaxial ferroelectric  $\text{Hf}_{0.5}\text{Zr}_{0.5}\text{O}_2$  thin films and their implementations in memristors for brain-inspired computing. *Adv. Funct. Mater.* **28**, 1806037 (2018).
- Estandía, S. et al. Engineering ferroelectric  $\text{Hf}_{0.5}\text{Zr}_{0.5}\text{O}_2$  thin films by epitaxial stress. *ACS Appl. Electron. Mater.* **1**, 1449–1457 (2019).
- Lu, H. et al. Enhancement of ferroelectric polarization stability by interface engineering. *Adv. Mater.* **24**, 1209–1216 (2012).

39. Yu, P. et al. Interface control of bulk ferroelectric polarization. *Proc. Natl Acad. Sci. USA* **109**, 9710–9715 (2012).
40. Shin, Y. J. et al. Interface control of ferroelectricity in an SrRuO<sub>3</sub>/BaTiO<sub>3</sub>/SrRuO<sub>3</sub> capacitor and its critical thickness. *Adv. Mater.* **29**, 1602795 (2017).
41. Chae, K. et al. Local epitaxial templating effects in ferroelectric and antiferroelectric ZrO<sub>2</sub>. *ACS Appl. Mater. Interfaces* **14**, 36771–36780 (2022).
42. Lyu, J., Fina, I., Solanas, R., Fontcuberta, J. & Sánchez, F. Robust ferroelectricity in epitaxial Hf<sub>1/2</sub>Zr<sub>1/2</sub>O<sub>2</sub> thin films. *Appl. Phys. Lett.* **113**, 082902 (2018).
43. Estandía, S., Dix, N., Chisholm, M. F., Fina, I. & Sánchez, F. Domain-matching epitaxy of ferroelectric Hf<sub>0.5</sub>Zr<sub>0.5</sub>O<sub>2</sub> (111) on La<sub>2/3</sub>Sr<sub>1/3</sub>MnO<sub>3</sub> (001). *Cryst. Growth Des.* **20**, 3801–3806 (2020).
44. Estandía, S. et al. Insights into the atomic structure of the interface of ferroelectric Hf<sub>0.5</sub>Zr<sub>0.5</sub>O<sub>2</sub> grown epitaxially on La<sub>2/3</sub>Sr<sub>1/3</sub>MnO<sub>3</sub>. *Phys. Rev. Mater.* **5**, 074410 (2021).
45. Cheema, S. S. et al. Emergent ferroelectricity in subnanometer binary oxide films on silicon. *Science* **376**, 648–652 (2022).
46. Gao, Z. et al. Identification of ferroelectricity in a capacitor with ultra-thin (1.5-nm) Hf<sub>0.5</sub>Zr<sub>0.5</sub>O<sub>2</sub> film. *IEEE Electron Device Lett.* **42**, 1303–1306 (2021).
47. Guo, R. et al. Interface-engineered electron and hole tunneling. *Sci. Adv.* **7**, eabf1033 (2021).
48. Pešić, M. et al. Physical mechanisms behind the field-cycling behavior of HfO<sub>2</sub>-based ferroelectric capacitors. *Adv. Funct. Mater.* **26**, 4601–4612 (2016).
49. Park, M. H. et al. Study on the size effect in Hf<sub>0.5</sub>Zr<sub>0.5</sub>O<sub>2</sub> films thinner than 8 nm before and after wake-up field cycling. *Appl. Phys. Lett.* **107**, 192907 (2015).
50. Kashir, A., Kim, H., Oh, S. & Hwang, H. Large remnant polarization in a wake-up free Hf<sub>0.5</sub>Zr<sub>0.5</sub>O<sub>2</sub> ferroelectric film through bulk and interface engineering. *ACS Appl. Electron. Mater.* **3**, 629–638 (2021).
51. Kashir, A., Oh, S. & Hwang, H. Defect engineering to achieve wake-up free HfO<sub>2</sub>-based ferroelectrics. *Adv. Eng. Mater.* **23**, 2000791 (2021).
52. Lyu, J. et al. Enhanced ferroelectricity in epitaxial Hf<sub>0.5</sub>Zr<sub>0.5</sub>O<sub>2</sub> thin films integrated with Si(001) using SrTiO<sub>3</sub> templates. *Appl. Phys. Lett.* **114**, 222901 (2019).
53. Chernikova, A. G. et al. Improved ferroelectric switching endurance of La-doped Hf<sub>0.5</sub>Zr<sub>0.5</sub>O<sub>2</sub> thin films. *ACS Appl. Mater. Interfaces* **10**, 2701–2708 (2018).
54. Lyu, J., Song, T., Fina, I. & Sánchez, F. High polarization, endurance and retention in sub-5 nm Hf<sub>0.5</sub>Zr<sub>0.5</sub>O<sub>2</sub> films. *Nanoscale* **12**, 11280–11287 (2020).
55. Spurgeon, S. R., Sushko, P. V., Chambers, S. A. & Comes, R. B. Dynamic interface rearrangement in LaFeO<sub>3</sub>/n-SrTiO<sub>3</sub> heterojunctions. *Phys. Rev. Mater.* **1**, 063401 (2017).
56. Varela, M. et al. Atomic-resolution imaging of oxidation states in manganites. *Phys. Rev. B* **79**, 085117 (2009).
57. Cao, T., Ren, G., Shao, D., Tsybmal, E. Y. & Mishra R. Stabilizing polar phase in binary metal oxides by hole doping. Preprint at <https://arxiv.org/abs/2209.09436> (2022).
58. Kresse, G. & Furthmüller, J. Efficient iterative schemes for ab initio total-energy calculations using a plane-wave basis set. *Phys. Rev. B* **54**, 11169–11186 (1996).
59. Blöchl, P. E. Projector augmented-wave method. *Phys. Rev. B* **50**, 17953–17979 (1994).
60. Perdew, J. P., Burke, K. & Ernzerhof, M. Generalized gradient approximation made simple. *Phys. Rev. Lett.* **77**, 3865–3868 (1996).

## Acknowledgements

This research is supported by A\*STAR RIE2020, Advanced Manufacturing and Engineering (AME) Programmatic Grant-A20G9b0135, the Singapore Ministry of Education MOE2018-T2-2-043, MOE-T2EP50121-0011, MOE Tier 1: 22-4888-A0001, A\*STAR AME IRG A1983c0036, the National Natural Science Foundation of China (12125407), the Zhejiang Provincial Natural Science Foundation (LD21E020002), the Joint Funds of the National Natural Science Foundation of China (U21A2067), and the National Key Research and Development Program of China (No. 2021YFA1500800). The research at the University of Nebraska-Lincoln was supported by the National Science Foundation through the EPSCoR RII Track-1 program (NSF Award OIA-2044049). W.L. thanks the support of the National Key R&D Program of China (Grant No. 2022YFA1602700), the National Natural Science Foundation of China (Grant No. 5227266), and the Natural Science Foundation of Jiangxi Province of China (Grant No.20224BAB201024).

## Author contributions

J.S.C., S.S., and W.L. conceived and designed the experiments. S.S. performed the thin film deposition, device fabrication, ferroelectric measurements, and data analysis. E.Y.T. and T.C. developed the theoretical concept. D.L., C.Z., and H.S. contributed to thin film deposition and device fabrication. J.N. and X.Y. contributed to the ferroelectric measurements. W.L., D.L., J.C., T.Z., and P.Y. contributed to the data analysis. H.X., Z.L., and H.T. performed the STEM experiments. S.S., E.Y.T., and J.S.C. wrote the manuscript and all authors contributed to its final version.

## Competing interests

The authors declare no competing interests.

## Additional information

**Supplementary information** The online version contains supplementary material available at <https://doi.org/10.1038/s41467-023-37560-3>.

**Correspondence** and requests for materials should be addressed to Xiaobing Yan, Evgeny Y. Tsybmal, He Tian or Jingsheng Chen.

**Peer review information** *Nature Communications* thanks Suraj Cheema and the other anonymous reviewer(s) for their contribution to the peer review of this work.

**Reprints and permissions information** is available at <http://www.nature.com/reprints>

**Publisher's note** Springer Nature remains neutral with regard to jurisdictional claims in published maps and institutional affiliations.

**Open Access** This article is licensed under a Creative Commons Attribution 4.0 International License, which permits use, sharing, adaptation, distribution and reproduction in any medium or format, as long as you give appropriate credit to the original author(s) and the source, provide a link to the Creative Commons license, and indicate if changes were made. The images or other third party material in this article are included in the article's Creative Commons license, unless indicated otherwise in a credit line to the material. If material is not included in the article's Creative Commons license and your intended use is not permitted by statutory regulation or exceeds the permitted use, you will need to obtain permission directly from the copyright holder. To view a copy of this license, visit <http://creativecommons.org/licenses/by/4.0/>.

© The Author(s) 2023